Processing and geometric attribute analysis of 3D PS-converted waves

Claudio D'Agosto and Kurt Marfurt, University of Houston, USA
Reinaldo J. Michelena, iReservoir.com, Littleton, Colorado, USA

Tury Taner defines seismic attributes as "all the information obtained from seismic data, either by direct measurements or by logic or experience-based reasoning." Seismic attributes typically provide information related to the amplitude, shape, and/or position of the seismic waveform. A common classification of seismic attributes consists of five categories: complex trace attributes, Fourier attributes, time attributes, windowed attributes, and geometric (also called multitrace) attributes. The last category consists of attributes calculated using more than one input seismic trace that provide quantitative information about lateral variations in the seismic data (including coherence, dip/azimuth, and amplitude gradients).

Geometric attributes, particularly seismic coherence, have been widely used in recent years to analyze 3D seismic data. However, most reports concern geometric attributes related to conventional 3D P-wave seismic data.

In this paper, we show examples of geometric attributes to analyze 3D PS-converted waves in land data from a carbonate reservoir in southwest Venezuela. We will focus on seismic coherence and principal component analysis. The coherence results are obtained from semblance and principal component estimates. Details about the calculation of these attributes can be found in Marfurt et al. (1998) and Gersztenkorn and Marfurt (1999).

We conclude that, in spite of the coarser bin size, PS reflections improve lateral resolution in coherence images in comparison with PP-reflections. The reason is a surprisingly broader recorded bandwidth for the PS waves, coupled with the lower S velocities and shorter wavelengths at any given frequency.

Overview of the area and acquisition geometry. The survey was conducted over a structurally simple, fractured carbonate reservoir at a depth of 3000 m. The main objective was to estimate fracture orientation and density in this carbonate which has a thickness of approximately 100 m and average velocity of 3000 m/s. The area covered by the seismic acquisition was about 25 km^2 and, in general, the data have a very good signal-to-noise ratio. Previous PS data in the area show the good quality of PS records (Ata and Michelena, 1995).

Figure 1 shows the acquisition geometry which has the following parameters: 720 fixed three-component geophones for a total of 2160 channels, with all channels live for each shot; 90 geophones per receiver line; 13 shot lines; 8 receiver lines; 54-m separation between shots; 40-m separation between receivers; 400-m separation between receiver lines; and 400-m separation between shot lines. The natural bin size for PP reflections for this recording geometry is 20 × 27 m. Explosive sources were used. The sampling rate was 2 ms and the record length was 8 s. This resulted in three data volumes corresponding to the vertical (Z), inline (H1), and crossline (H2) components.

Figure 2 shows the fold distribution for both PP and PS reflections. The bin size for PP data is 20 × 27 m; the bin size for PS data is 36 × 27 m (assuming an average V_P/V_S ratio of 2 for this area). Notice how the fold distribution for both PP and PS data is even across the survey.

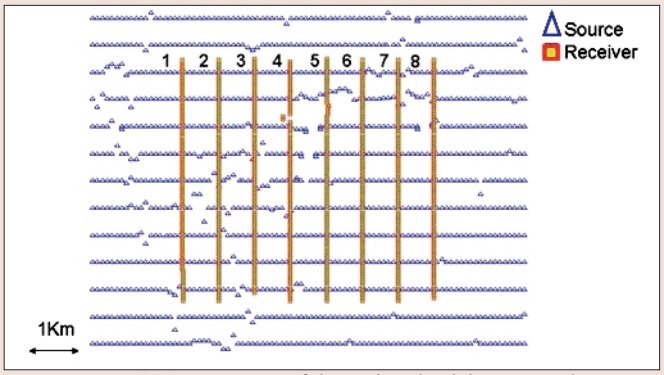

Figure 1. Acquisition geometry of the 3D/3-C land data set. Red squares indicate receiver positions and blue triangles indicate shot positions.

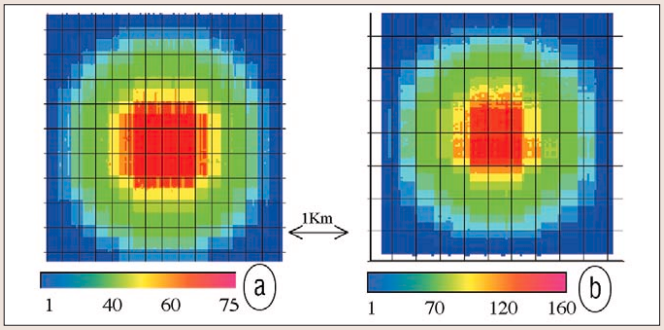

Figure 2. Fold distribution map for (a) PP reflections and (b) PS reflections. Bin size for PP data is 20 × 27 m. Bin size for PS data is 36 × 27 m.

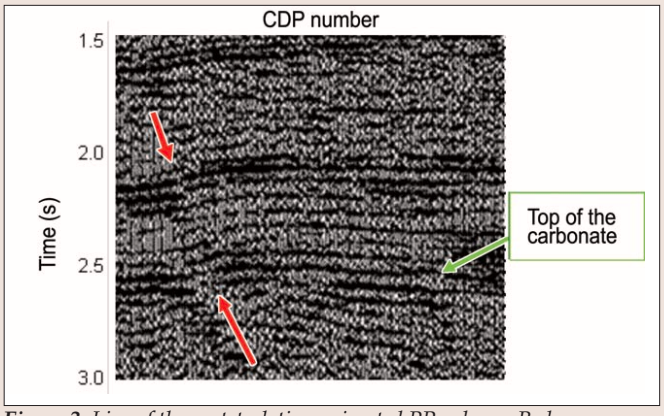

Figure 3. Line of the poststack time-migrated PP volume. Red arrows indicate the reverse fault.

Seismic processing of the vertical component for PP reflections. The data have good signal-to-noise ratio. Reflectors are well defined and continuous across the data volume. We identified two components in the ground roll noise cone: A faster component with a velocity of approximately 500 m/s and a slower component with a velocity of approximately 300 m/s. Both noise trains are aliased, making attenuation by *f-k* techniques problematic.

The dominant frequency of the ground roll is 8 Hz and this energy is much stronger than the reflected signal (domi-

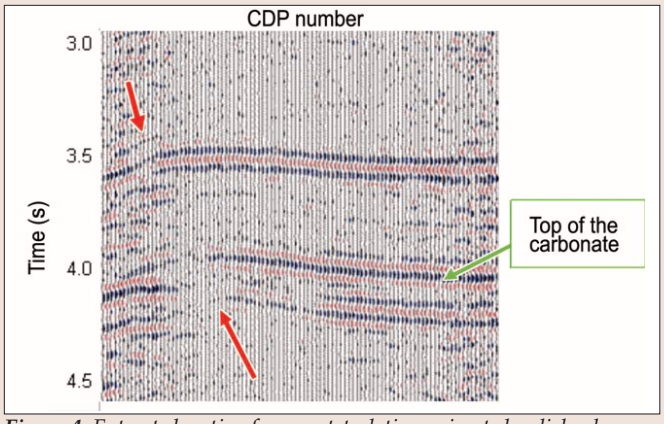

Figure 4. Extracted section from poststack time-migrated radial volume. Red arrows indicate the reverse fault. These data correspond to Figure 3, and were generated considering all azimuths and offsets.

nant frequency of 18 Hz). In order to reduce the ground roll, we applied a linear moveout followed by an *f-k* filter and inverse linear moveout to restore the original record times. To remove the low-frequency component, we applied a band-pass filter (10, 15, 40, 60) that preserves the frequency content of the reflectors and attenuates the residual low-frequency component of the ground roll.

Next, we performed velocity analysis to obtain the stacking velocities needed to build a brute stack. These stacking velocities were used for residual statics estimation and as the velocity model for prestack time migration. Stacking velocities have small lateral variations. Figure 3 shows a line of the poststack time-migrated radial volume.

Seismic processing of the horizontal components for PS reflections. The processing sequence for the horizontal components of the 3D/3-C data set consisted of corrections for polarization, asymptotic CCP binning, modeling to remove ground roll, surface-consistent gain, surface-consistent deconvolution, residual statics, velocity analysis, and poststack time migration.

Model-driven filtering enhances the imaging of the deep reflectors without significantly altering their amplitudes and therefore facilitates velocity analysis and improves the stack results. Figure 4 shows a line of the poststack time-migrated radial volume.

Geometric attributes applied to PP data. We then calculated geometric attributes and extract them along the top of the carbonate formation at 2.6 s (Figure 3). Figure 5a shows a horizon slice of the principal component coherence cube estimated on the PP volume. The main NS fault (blue arrows, shown in Figures 3 and 4) is easily identified and appears to splay into a set of parallel faults to the north. Another fault system, oriented NE-SW, is indicated by green arrows. Figure 5b shows the semblance coherence at the same time slice. The patterns are consistent with Figure 5a but of lower resolution. Since we used a nine-trace analysis window, the eigenvector is directly related to the spatial variation of the most coherent part of the seismic amplitudes. Figures 5c and 5d are plots of the east and north gradients of the principal component eigenvector. Observe that the east gradient of the eigenvectors enhances the NS features and shows a complementary display of the incoherent events observed in the principal component and semblance coherence volumes. Here it is possible to identify some SE-NW lineations, which form a conjugate system to the previously identified NE-SW lineations. Some clear lineations, oriented NS, associated with acquisition footprint are indicated with red arrows. Figure 5d displays the

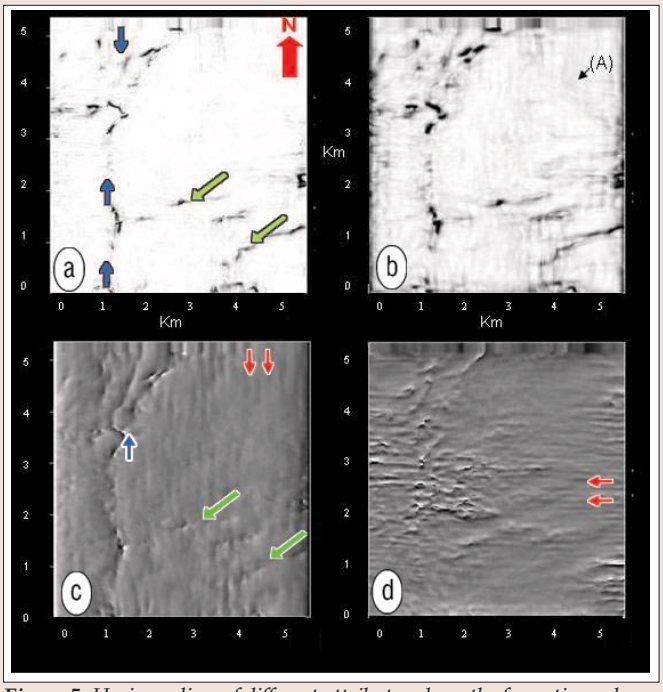

Figure 5. Horizon slices of different attributes along the formation calculated from the PP (vertical component) data volume: (a) principal component coherence; (b) semblance coherence; (c) east gradient of the principal component eigenvector; (d) north gradient of principal component eigenvector. Red arrows in (c) and (d) indicate acquisition footprints. Blue arrows in (a) and (c) indicate the reverse fault in Figure 3. Fault system (NE-SW) indicated by green arrows in (a) and (c).

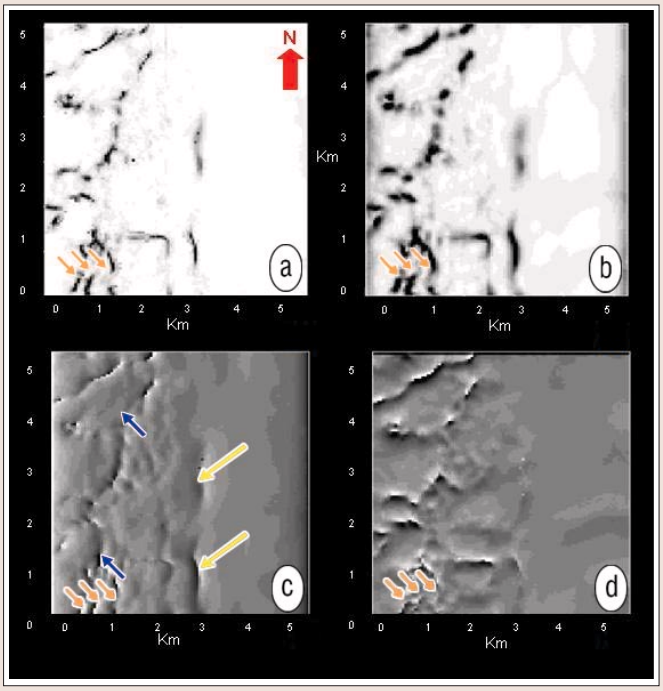

Figure 6. Horizon slices of different attributes along the formation calculated from all azimuths and offsets of the PS (radial component) data volume: (a) principal component coherence; (b) semblance coherence; (c) east gradient of the principal component eigenvector; (d) north gradient of principal component eigenvector. Blue arrows in (c) indicate the reverse fault in Figure 4. Yellow arrows in (c) indicate a NS lineation not present in PP attribute maps.

north gradient of the eigenvector which enhances lateral resolution of features in the EW direction and indicates faults running parallel to the main NS fault. The EW lineations (red arrows) are acquisition footprint.

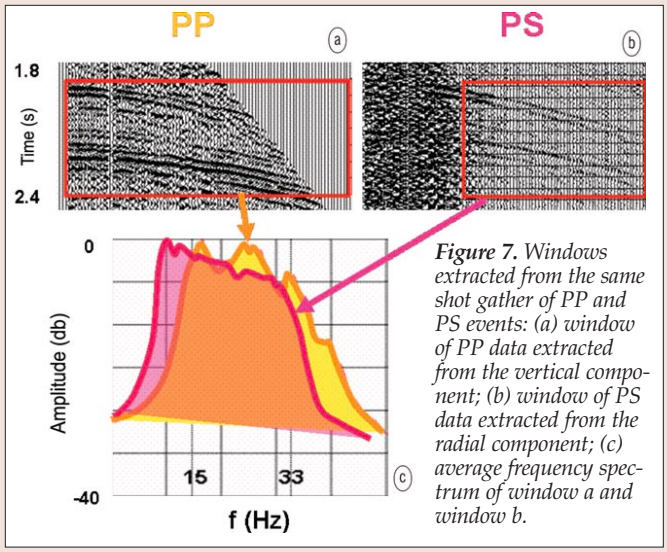

Figure 7. Windows extracted from the same shot gather of PP and PS events: (a) window of PP data extracted from the vertical component; (b) window of PS data extracted from the radial component; (c) average frequency spectrum of window a and window b.

Geometric attributes applied to PS data. We repeated the analysis for the vertical component PP reflection volume to the radial component PS reflection volume. We calculated geometric attributes and extracted them along the horizon related to the top of the formation of interest (at 4.1 s in Figure 4). We began with a cube containing all azimuths and offsets. Figure 6 displays horizon extractions of the same attributes shown in Figure 5 but generated from the radial component of the PS data volume for full azimuth and offset. The PS reflections to identify parallel faults (orange arrows) at the southern end of the main NS fault that were not imaged by PP reflections. We observe in general that the attributes generated from PS data give better resolution, in the sense that they can better image faults, than the PP attributes.

This is because PS waves have longer traveltimes than PP waves due to the fact that the former travel as P-waves from the source to the point where they convert to lower velocity S-waves which increases the traveltime. This effect produces a more evident time shift in a fault on a seismic section (separation between upper block and lower block) for PS waves than PP waves and allows the coherence algorithm to detect a change in continuity (coherence) in PS waves that is not recognizable in PP waves.

Figure 6a shows a horizon slice of the principal component coherence cube estimated on the PS volume. Figure 6b shows the semblance coherence at the same time slice. The patterns are consistent with those obtained with principal component coherence. Since we used a nine-trace analysis window, the eigenvector is directly related to the spatial variation of the most coherent part of the seismic amplitudes. Figures 6c and 6d plot the east and north gradient of the principal component eigenvector; observe that the east gradient of the eigenvectors enhances the NS features.

While in general the PS attributes exhibit greater lateral resolution than the PP attributes, they have not illuminated the NE-SW fault trend seen on the PP data. The reason could be differences between P- and S-wave reflectivity, or in the angles of illumination. We observed that results obtained with the radial component seem less susceptible to acquisition footprint than attributes obtained from PP data (the acquisition footprint is shown in the PP data by red arrows in Figure 5).

We also noticed the presence of a NS lineation in the middle of the PS coherence attribute extractions (yellow arrows in Figure 6c) that is not present in the in the PP data. Careful examination of the radial component over different azimuths shows that this lineation (Figure 6c) can be explained as a pinchout (D'Agosto, 2003).

In general, shear waves are attenuated faster than P waves. At the study area, the highest frequency recorded in the PS data is still comparable to that of the PP data (Figure 7). For this data set, the central frequency of the P-waves (18 Hz) is slightly higher than the central frequency of the S-waves (10 Hz) even though the bandwidth for shear waves is larger than the bandwidth for P-waves. Therefore, the larger bandwidth of the PS-waves is another reason that converted waves have better lateral resolution than compressional waves. Figure 7a shows a time window extracted from the vertical component before processing. Figure 7c plots its frequency spectrum. Figure 7b is a time window from the radial component of the same receiver line and its frequency spectrum is shown in Figure 7c. The bandwidth for the vertical component is approximately 1.1 octaves, whereas the bandwidth for the radial component is approximately 1.8 octaves. Hence the frequency bandwidth, and therefore time resolution, is greater for converted waves than for the PP waves.

Conclusions. The gradient of the eigenvector attribute gives a considerably more detailed image of the features than the coherence attributes for PP or PS seismic data. The radial component is less susceptible to acquisition footprints. The east gradient of the eigenvectors enhances the NS features and the north gradient of the eigenvectors enhances the EW features for PP and PS data.

The longer traveltime of the PS waves than PP waves and the larger bandwidth of the frequency spectrum of PS waves than PP waves cause converted waves to have better vertical resolution than PP waves. For this study area both elements were present.

These results suggest that structural attributes derived from PS waves can lead to better imaging of structural patterns than those derived from PP waves.

For this study area, the PS volume has higher vertical resolution than the corresponding PP volume, and thereby allows us to observe greater detail. Furthermore, the frequency bandwidth, and therefore time resolution, is greater for converted waves than for the PP waves.

Suggested reading. *Interpretation of Three Dimensional Seismic Data* by Brown (AAPG, 2001). "3D seismic discontinuity for faults and stratigraphic features: The coherence cube" by Bahorich and Farmer (*TLE*, 1995). "Birefringence analysis at Borburata field for fracture characterization" by D'Agosto (master's thesis, University of Houston, 2003). "Modeling and removal of ground roll from horizontal component of C-waves" by D'Agosto et al. (SEG 2003 *Expanded Abstracts*). "Eigenstructure-based coherence computations as an aid to 3D structural and stratigraphic mapping" by Gersztenkorn and Marfurt (GEOPHYSICS, 1999). "3D seismic attributes using a semblance-based coherency algorithm" by Marfurt et al. (GEOPHYSICS, 1998). *Attributes Revisited* by Taner (2000, available at *http://www.rocksolidimages.com/pdf/attrib_revisited.htm*). "Mapping distribution of fractures in a reservoir with PS concerted waves" by Ata and Michelena (*TLE*, 1995). TLE

Acknowledgments: Thanks to Geocenter for providing the University of Houston with the seismic processing software SeisUP and for helpful comments about this work. Thanks to PDVSA for support. We thank our colleagues at the Stanford Exploration Project. Many displays in this paper used their graphic programs and all our internal processing algorithms are written on their SEPlib framework. Claudio D'Agosto is now with Eni E&P in Milan, Italy.

Corresponding author: michelena@ireservoir.com